A waveguide-typed plasmonic mode converter

Hae-Ryeong Park,[1,2] Jong-Moon Park,[2] Min-su Kim,[3] and Myung-Hyun Lee[1,*]

[1]*School of Electronic and Electrical Engineering, Sungkyunkwan University, Suwon, Gyeonggi-Do, 440-746, South Korea*

[2]*CAE Team, LCD R&D Center, LCD Business, Samsung Display Co. Ltd., San #24 Nongseo-Dong, Giheung-Gu, Yongin-City, Gyeonggi-Do, 446-711, South Korea*

[3]*Electronics & Telecommunications Research Institute, 161 Gajong-dong, Yusong-gu, Daejeon 305-701, South Korea*

[*]*mhlee@skku.edu*

Abstract: Waveguide-typed plasmonic mode converters (WPMCs) at a wavelength of 1.55 μm are presented. The WPMC is composed of an insulator-metal-insulator waveguide (IMI-W), a 1st reversely tapered insulator-metal-insulator-metal-insulator waveguide (RT-IMIMI-W), an insulator-metal-insulator-metal-insulator waveguide (IMIMI-W), a 2nd RT-IMIMI-W with lateral silver mirrors (LSMs), and a metal-insulator-metal waveguide (MIM-W) in series. The mode sizes for the IMI-W, IMIMI-W, and MIM-W via the IMIMI-W with LSMs were not only calculated using a finite element method but were also experimentally measured. The input mode size of 10.3 μm × 10.3 μm from a polarization-maintaining single-mode fiber was squeezed to the mode size of ~2.9 μm × 2.9 μm in measurement by converting an s_0 mode to an Sa_0 mode via an Ss_0 mode. The WPMC may be potentially useful for bridging micro- to nano-plasmonic integrated circuits.

OCIS codes: (240.6680) Surface plasmons; (250.5403) Plasmonics; (160.5470) Polymers; (130.3120) Integrated optics devices.

References and links

1. H. Raether, *Surface Plasmons* (Springer-Verlag, 1988).
2. W. L. Barnes, A. Dereux, and T. W. Ebbesen, "Surface plasmon subwavelength optics," Nature **424**(6950), 824–830 (2003).
3. N. Fang, H. Lee, C. Sun, and X. Zhang, "Sub-diffraction-limited optical imaging with a silver superlens," Science **308**(5721), 534–537 (2005).
4. M. I. Stockman, "Nanoplasmonics: past, present, and glimpse into future," Opt. Express **19**(22), 22029–22106 (2011).
5. M. E. Stewart, C. R. Anderton, L. B. Thompson, J. Maria, S. K. Gray, J. A. Rogers, and R. G. Nuzzo, "Nanostructured Plasmonic Sensors," Chem. Rev. **108**(2), 494–521 (2008).
6. S. A. Maier, "Plasmonics: Metal nanostructures for subwavelength photonic devices," IEEE J. Sel. Top. Quantum Electron. **12**(6), 1214–1220 (2006).
7. R. Zia, J. A. Schuller, A. Chandran, and M. L. Brongersma, "Plasmonics: the next chip-scale technology," Mater. Today **9**(7-8), 20–27 (2006).
8. J. A. Dionne, L. A. Sweatlock, H. A. Atwater, and A. Polman, "Plasmon slot waveguides: Towards chip-scale propagation with subwavelength-scale localization," Phys. Rev. B **73**(3), 035407 (2006).
9. L. Liu, Z. Han, and S. He, "Novel surface plasmon waveguide for high integration," Opt. Express **13**(17), 6645–6650 (2005).
10. P. Ginzburg and M. Orenstein, "Plasmonic transmission lines: from micro to nano scale with λ/4 impedance matching," Opt. Express **15**(11), 6762–6767 (2007).
11. P. Ginzburg, D. Arbel, and M. Orenstein, "Gap plasmon polariton structure for very efficient microscale-to-nanoscale interfacing," Opt. Lett. **31**(22), 3288–3290 (2006).
12. S. Zhu, T. Y. Liow, G. Q. Lo, and D. L. Kwong, "Fully complementary metal-oxide-semiconductor compatible nanoplasmonic slot waveguides for silicon electronic photonic integrated circuits," Appl. Phys. Lett. **98**(2), 021107 (2011).
13. R. Yang, M. A. G. Abushagur, and Z. Lu, "Efficiently squeezing near infrared light into a 21 nm-by-24 nm nanospot," Opt. Express **16**(24), 20142–20148 (2008).

#169659 - $15.00 USD Received 1 Jun 2012; revised 10 Jul 2012; accepted 24 Jul 2012; published 31 Jul 2012

14. R. Zia, M. D. Selker, P. B. Catrysse, and M. L. Brongersma, "Geometries and materials for subwavelength surface plasmon modes," J. Opt. Soc. Am. A **21**(12), 2442–2446 (2004).
15. P. Berini, "Plasmon-polariton waves guided by thin lossy mrtal films of finite width: Bound modes of symmetric structures," Phys. Rev. B **61**(15), 10484–10503 (2000).
16. P. Berini, "Long-range surface plasmon polaritons," Adv. Opt. Photon. **1**(3), 484–588 (2009).
17. W.-J. Lee, J.-E. Kim, H. Y. Park, S. Park, J.-M. Lee, M.- Kim, J. J. Ju, and M.-H. Lee, "Enhanced transmission in a fiber-coupled Au stripe waveguide system," IEEE Photon. Technol. Lett. **22**(2), 100–102 (2010).
18. J. J. Ju, S. Park, M.- Kim, J. T. Kim, S. K. Park, Y. J. Park, and M.-H. Lee, "Polymer-based long-range surface plasmon polariton waveguides for 10-Gbps optical signal transmission applications," J. Lightwave Technol. **26**(11), 1510–1518 (2008).
19. S. Park, J. J. Ju, J. T. Kim, M. S. Kim, S. K. Park, J.-M. Lee, W.-J. Lee, and M.-H. Lee, "Sub-dB/cm propagation loss in silver stripe waveguides," Opt. Express **17**(2), 697–702 (2009).
20. S. Park, M.- Kim, J. T. Kim, S. K. Park, J. J. Ju, and M.-H. Lee, "Long range surface plasmon polariton waveguides at 1.31 and 1.55 μm wavelengths," Opt. Commun. **281**(8), 2057–2061 (2008).
21. S. Park, M.- Kim, J. J. Ju, J. T. Kim, S. K. Park, J.-M. Lee, W.-J. Lee, and M.-H. Lee, "Temperature dependence of symmetric and asymmetric structured Au stripe waveguides," Opt. Commun. **283**(17), 3267–3270 (2010).
22. P. Berini, R. Charbonneau, N. Lahoud, and G. Mattiussi, "Characterization of long-ranging surface-plasmon-polariton waveguides," J. Appl. Phys. **98**(4), 043109 (2005).
23. A. Boltasseva, T. Nikolajsen, K. Leosson, K. Kjaer, M. S. Larsen, and S. I. Bozhevolnyi, "Integrated optical components utilizing long-range surface plasmon polaritons," J. Lightwave Technol. **23**(1), 413–422 (2005).
24. R. Charbonneau, N. Lahoud, G. Mattiussi, and P. Berini, "Demonstration of integrated optics elements based on long-ranging surface plasmon polaritons," Opt. Express **13**(3), 977–984 (2005).
25. H.-R. Park, M.- Kim, I.-S. Jeong, J.-M. Park, J. J. Ju, and M.-H. Lee, "Nanoimprinted Bragg gratings for long-range surface plasmon polaritons fabricated via spin coating of a transparent silver ink," IEEE Trans. NanoTechnol. **10**(4), 844–848 (2011).
26. D. Woolf, M. Loncar, and F. Capasso, "The forces from coupled surface plasmon polaritons in planar waveguides," Opt. Express **17**(22), 19996–20011 (2009).
27. H.-R. Park, J.-M. Park, M. S. Kim, J. J. Ju, J.-H. Son, and M.-H. Lee, "Effective plasmonic mode-size converter," Opt. Express **19**(22), 21605–21613 (2011).
28. M.-H. Lee, "Long-range surface plasmon polariton waveguides containing very thin spin-coated silver films," Thin Solid Films **519**(18), 6097–6101 (2011).
29. InkTec Co, Ltd., Available: http://www.inktec.com
30. E. D. Palik, ed., *Handbook of Optical Constants of Solids* (Academic, New York, 1985).
31. ChemOptics, Inc., Available: http://www.chemoptics.co.kr
32. W.-J. Lee, J.-E. Kim, H. Y. Park, S. Park, M.- Kim, J. T. Kim, and J. J. Ju, "Optical constants of evaporated gold films measured by surface plasmon resonance at telecommunication wavelengths," J. Appl. Phys. **103**(7), 073713 (2008).
33. C. O. M. S. O. L. Multiphysics, Inc., Available: http://www.comsol.com.
34. FDTD and MODE Solutions, Lumerical Solutions Inc., Available: http://www.lumerical.com
35. H.-R. Park, "Investigation of hybrid plasmonic waveguides for nano-scale optical focusing and propagation," Ph. D thesis, Sungkyunkwan University (2011).
36. J. P. Berenger, "A perfectly matched layer for the absorption of electromagnetic waves," J. Comput. Phys. **114**(2), 185–200 (1994).

1. Introduction

The lowest physical dimension of optic elements is basically determined by the diffraction limit of the light used, and this scale is about half of its wavelength. Recently, surface plasmon polaritons (SPPs) have attracted much interest since they can overcome the diffraction limit of light. SPPs are transverse magnetic (TM) polarized waves propagating on an interface between a metal and a dielectric [1]. The SPPs arise from interactions between evanescent electromagnetic fields and longitudinal collective oscillations of the free electrons in metals. In general, SPPs support mode properties in diverse structures. Therefore, SPPs have been widely studied for use in micro- to nano-photonic applications [2–13].

A symmetric mode of magnetic fields with respect to the center of the metal, i.e., long-range SPPs (LR-SPPs), can be formed on insulator-metal-insulator waveguides (IMI-Ws) [14–16]. By controlling the width and the thickness of the metal stripe, the mode-field size of the LR-SPP can be easily adjusted to be close to that of a single-mode fiber (SMF) [17–21]. Therefore, the LR-SPP can be efficiently excited by a butt-coupling method. The propagation length of the LR-SPP dramatically increases with decreasing metal thickness [18, 20, 22, 23]. For these reasons, experimental studies of LR-SPP components including modulators, switches, Y-junctions, directional couplers, and Bragg gratings have been widely demonstrated [23–25]. On the other hand, metal-insulator-metal waveguides (MIM-Ws) support a symmetrically coupled mode of magnetic fields with respect to the central insulator layer, which is known as the gap-SPP (G-SPP) mode [14, 26]. This gap-SPP mode offers high confinement of the electromagnetic field in the insulator layer compared to the LR-SPP mode in the IMI-W. The G-SPP mode can be propagated up to the micron scale length with a nano-scale mode-field size by properly adjusting the thickness of the insulator [13]. Therefore, mode confinement below the diffraction limit in the MIM-W can be realized in highly integrated photonic devices.

Recently, a more complex multilayered configuration referred to as the insulator-metal-insulator-metal-insulator waveguide (IMIMI-W) has been studied to take advantage of both IMI-W and MIM-W [27]. In IMIMI-W, the symmetric LR-SPP mode, which is formed by symmetrical coupling between the LR-SPP modes in each metal layer, offers a relatively small mode-field size compared to the LR-SPP mode in the IMI-W. On the other hand, the symmetric short-range SPP (SR-SPP) mode, which is formed by symmetrical coupling between the antisymmetric modes (SR-SPP modes) in each metal layer, supports a sub-wavelength-size mode similar to the G-SPP mode in the MIM-W. The IMIMI-W can offer hybrid integration and effective mode conversion between the IMI-W and the MIM-W, which offers the benefits of high integration and easy fabrication for more complex plasmonic device geometries. In hybrid integration, coupling loss occurs due to mismatch in the mode-size and in the mode-index of different SPP structures. The coupling loss can be easily minimized by inserting a tapered waveguide which is generally used to minimize mismatches between photonic and/or plasmonic waveguides [17, 27]. With an efficient mode matching element, the IMIMI-Ws may be applicable for bridging from micro- to nano-photonic integrated circuits.

In this paper, we demonstrate waveguide-typed plasmonic mode converters (WPMCs) at a wavelength suitable for telecommunications. The structure was successively composed of an input IMI-W to reduce the coupling loss with a polarization-maintaining SMF (PMSMF), a 1st reversely tapered IMIMI-W (RT-IMIMI-W) to convert the s_0 mode to the Ss_0 mode, a straight IMIMI-W, a 2nd RT-IMIMI-W with lateral silver mirrors (LSMs) to focus the Ss_0 mode laterally and to convert the Ss_0 mode to the Sa_0 mode at the same time, and an MIM-W to stabilize the converted Sa_0 mode. A thermal evaporated gold (Au), low-loss polymer materials and transparent silver ink were used for WPMCs. The optical characteristics of each component in the designed WPMC were simulated and analyzed. In addition, the optical characteristics of each component in the fabricated WPMC were experimentally measured and compared.

This paper is organized as follows. In Sections 2 and 3, the design and fabrication processes of the WPMC are described in detail. The results and discussions are presented in Section 4, while concluding remarks are summarized in Section 5.

2. Details in design

There are two parts of the proposed WPMC. One is an s_0 to Ss_0 mode converter, called an reverse-type plasmonic mode size converter (R-PMSC) because it adopt a reverse taper instead of the forward taper used in the PMSC [27]. The other is an Ss_0 to Sa_0 mode converter, called an Sa_0 mode converter (Sa_0MC). Figure 1 shows the structure of the WPMC, consisting of the R-PMSC and the Sa_0MC. The 41.65μm-long R-PMSC is successively composed of an input 40 μm-long IMI-W and a 1.65μm-long 1st RT-IMIMI-W. In the input region, in order to reduce the coupling loss between a PMSMF and the input IMI-W, the width and thickness of the Au strip in the input IMI-W were designed to be 5 μm and 20 nm, respectively [18]. In the 1st RT-IMIMI-W region, in order to convert the s_0 mode in the IMI-W to an Ss_0 mode in the IMIMI-W efficiently, the 1st RT-IMIMI-W was designed to have widths of 1.3 μm and 1.7 μm at both ends with a length of 1.65 μm. The thicknesses of the

#169659 - $15.00 USD Received 1 Jun 2012; revised 10 Jul 2012; accepted 24 Jul 2012; published 31 Jul 2012

upper and lower Au strips are 20 nm each. The thickness of the central insulator in the 1st RT-IMIMI-W was designed to be 500 nm.

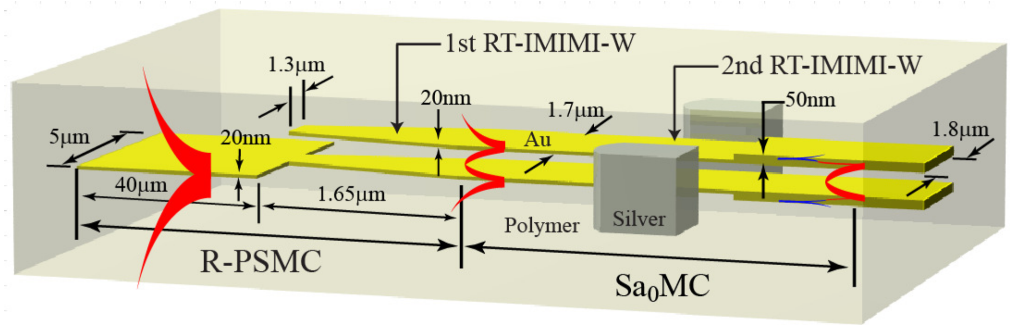

Fig. 1. Schematic view of the proposed WPMC, which is composed of the input IMI-W, the 1st RT-IMIMI-W, the straight IMIMI-W, the 2nd RT-IMIMI-W with the LSMs, and the output MIM-W in series. The total length of the proposed WPMC is 53.65 μm including the 41.65μm-long R-PMSC and the 12 μm-long Sa_0MC. The 1.65 μm-long 1st RT-IMIMI-W is exaggerated in this view.

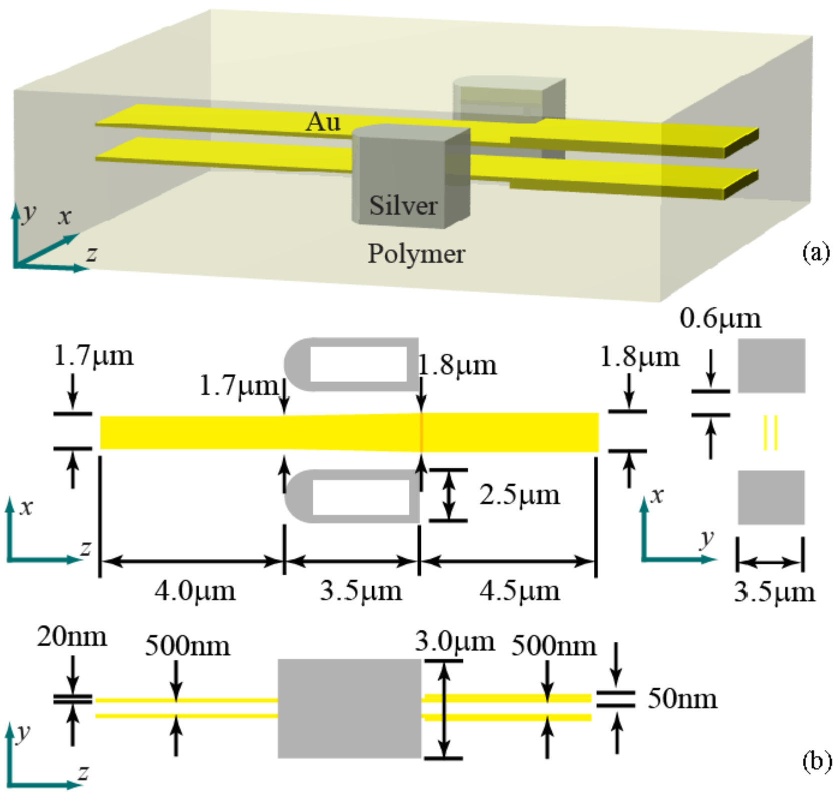

Fig. 2. (a) Schematic view of the proposed Sa_0MC and (b) its detailed design parameters at the top and side views. The outer shells of the LSMs are made of a transparent silver ink and the inside of the LSMs is filled with a low-loss polymer.

Figure 2 shows the structure of the Sa_0MC which consists of the straight IMIMI-W, a 2nd RT-IMIMI-W with two LSMs, and an output MIM-W successively. The straight 1.7 μm-wide IMIMI-W was designed with a length of 4.0 μm to stabilize the converted Ss_0 mode. To simultaneously focus the stabilized Ss_0 mode laterally while also converting the Ss_0 mode to

Received 1 Jun 2012; revised 10 Jul 2012; accepted 24 Jul 2012; published 31 Jul 2012

the Sa_0 mode, the 2nd RT-IMIMI-W with the LSMs was designed with a length of 3.5 μm. The widths of the 2nd RT-IMIMI-W were designed to be 1.7 μm and 1.8 μm at both ends as shown in Fig. 2. Again, the thicknesses of the upper and lower strips in the IMIMI-Ws are 20 nm. Two LSMs are located at both sides of the 2nd RT-IMIMI-W in the Sa_0MC. The gap between the 2nd RT-IMIMI-W and the LSMs is 0.6 μm. The shape of the LSM is a semicylinder prism which is composed of a hemisphere and a square column as shown in Fig. 2. The height, width and length of the LSMs are 3.0, 2.5 and 3.5 μm, respectively. The straight 1.8 μm-wide MIM-W with a length of 4.5 μm was designed to both cut off the Ss_0 mode vertically and stabilize the converted Sa_0 mode. The thicknesses of the upper and lower strips in the MIM-W are 50 nm. The designed length of the Sa_0MC is 12 μm. The thickness of the central insulator in both the IMIMI-Ws and the MIM-W was designed to be 500 nm. All the strips and insulators in the IMI-W, the RT-IMIMI-Ws, the IMIMI-W, and the MIM-W are made of an evaporated Au and a low-loss polymer. The outer shells of LSMs are made of a transparent silver ink [20, 28]. The inside of the LSMs is filled with the low-loss polymer. Here, the refractive indices of the low-loss polymer, the evaporated Au, the silver ink film are 1.450, 0.550 −11.4912i and 0.7104 −7.1112i, respectively at the wavelength of 1.55 μm [29–32].

The 20 nm-thick IMI-W supports two modes: a symmetric mode (s_0, where the subscript 0 indicates the fundamental mode), and an antisymmetric mode (a_0). Here, the mode symmetry is defined from the field distribution of the transverse magnetic field component (H_x) in the structure. However, the 20 nm-thick IMI-W with a width less than 1.7 μm cannot support the s_0 mode as shown in Fig. 3(a). The 20 nm-thick and 500 nm-gap IMIMI-W supports two symmetric modes (Ss_0, Sa_0) and two antisymmetric modes (As_0, Aa_0) [14, 17]. However, the 20 nm-thick IMIMI-Ws with a width less than 1.7 μm cannot support the Sa_0 mode as shown in Fig. 3(a). Again, the 50 nm-thick and 500 nm-gap MIM-W supports two symmetric modes (Ss_0, Sa_0) and two antisymmetric modes (As_0, Aa_0). The Ss_0 mode has optical properties similar to the s_0 mode including propagation loss, mode-field size, and mode shape. The optical properties of the Sa_0 mode are similar to the G-SPP mode in the MIM waveguide [8, 11, 13, 14, 27]. In this study, we focused on squeezed mode conversion from an s_0 mode to an Sa_0 mode via an Ss_0 mode. Therefore, only the s_0, Ss_0, Sa_0 modes are mentioned here.

Figures 3(a) and 3(b) show the effective refractive indices and the horizontal and vertical mode sizes of the s_0, Ss_0, and Sa_0 modes as a function of the width, which were calculated with a finite element method (FEM) of COMSOL Multiphysics [33] and a MODE solution of Lumerical, Inc [34]. The thicknesses of the Au strips in the IMI-Ws and IMIMI-Ws are fixed with 20 nm, and the thicknesses of the central insulator in the IMIMI-Ws are also fixed with 500 nm in this calculation. The s_0 mode can be excited in the 5 μm-wide IMI-W while the Ss_0 and Sa_0 modes can be excited in the IMIMI-W. At a width less than 1.7 μm, the s_0 mode and the Sa_0 mode cannot be excited, but the Ss_0 mode can be excited in the IMIMI-W as shown in Fig. 3(a). To couple the PMSMF mode effectively, the 5 μm-wide IMI-W was introduced as the input SPP waveguide because the effective refractive index and the mode size of its s_0 mode are similar to those of the PMSMF mode [18]. The coupling loss between the PMSMF and the 5 μm-wide IMI-W is estimated to be 0.8 dB/facet by using MODE solution [34]. Here, the input mode size of 10.3 μm × 10.3 μm was used for PMSMF. The s_0 mode-field size in the 5 μm-wide IMI-W is 8.1 μm × 7.0 μm (horizontal × vertical) in simulation. To convert the s_0 mode to an Ss_0 mode efficiently, the 1.3 μm-wide IMIMI-W was designed at the converting region in Fig. 1 because the effective refractive index and the mode size of the s_0 mode in the 5 μm-wide IMI-W are also similar to those of the Ss_0 mode in the 1.3 μm-wide IMIMI-W as shown in Fig. 3. The simulated loss for the s_0 to Ss_0 mode conversion is 1.2 dB. The 1st RT-IMIMI-W was designed to prepare the Ss_0 to Sa_0 mode conversion because the mode size of the Ss_0 mode can be squeezed by varying the width of IMIMI-W from 1.3 μm to

#169659 - $15.00 USD Received 1 Jun 2012; revised 10 Jul 2012; accepted 24 Jul 2012; published 31 Jul 2012

1.7 μm and there was no Sa_0 mode in the 1.3 μm-wide IMIMI-W. The Ss_0 mode-field size in the 1.7 μm-wide IMIMI-W is 3.4 μm × 3.2 μm in simulation.

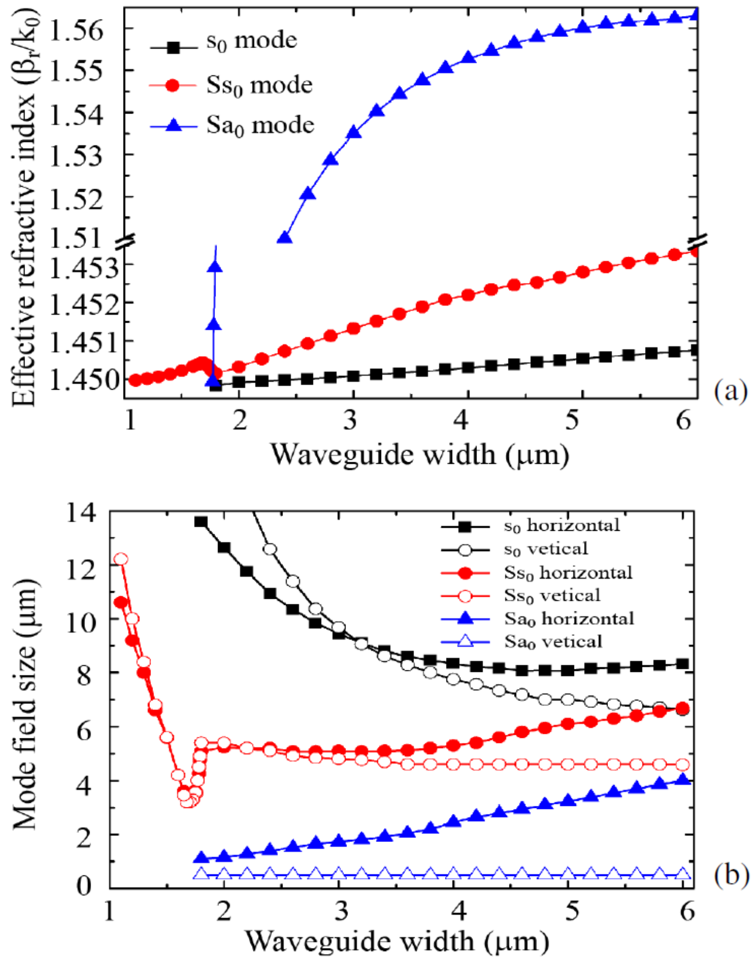

Fig. 3. (a) Effective indices and (b) the horizontal and vertical mode sizes for the s_0 mode in the 20 nm-thick IMI-W, Ss_0 mode and Sa_0 mode in the 20 nm-thick and 500 nm-gap IMIMI-W as a function of the waveguide width.

The 1.7 μm-wide, 4 μm-long, 20 nm-thick, and 500 nm-gap IMIMI-W only supports the Ss_0 mode. The charge distribution, E_z field, and intensity of the Ss_0 mode are schematically shown in Figs. 4(a)–4(c). At the beginning of the 2nd RT-IMIMI-W with the LSMs, the Ss_0 mode becomes squeezed and turned to become similar to the charge distribution of the Sa_0 mode due to the semicylinder shaped prisms in the LSMs. However, the E_z field is still similar to that of the Ss_0 mode, as shown in Figs. 4(d)–4(f). With increasing the width of the LSMs and the width of the 2nd RT-IMIMI-W from 1.7 to 1.8 μm, the Sa_0 mode becomes formed as shown in Figs. 4(g)–4(i). The Sa_0 mode that formed at the end of the 2nd RT-IMIMI-W finally stabilizes through the 1.8 μm-wide MIM-W with the 50 nm-thick Au strips of a 500 nm-gap. The simulated Sa_0 mode size in the 1.8 μm-wide IMIMI-W is 1.1 μm × 0.5μm. The simulated loss for the Ss_0 to Sa_0 mode conversion is 5.2 dB.

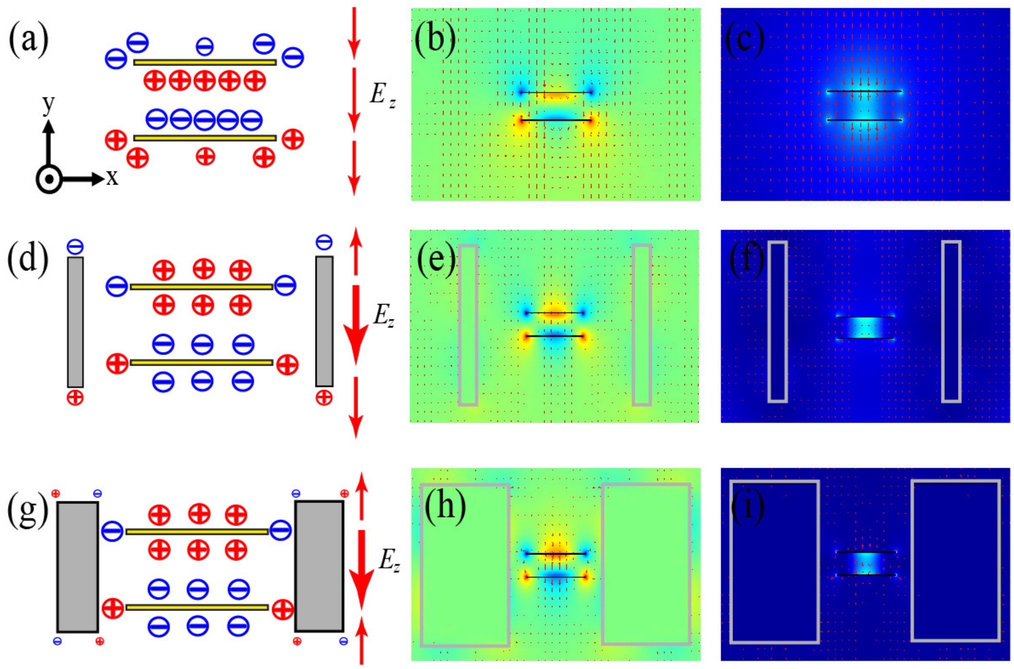

Fig. 4. (a)-(c): Charge distribution, E_z field and mode-intensity in the propagation direction for the Ss_0 mode in the 1.7 μm-wide IMIMI-W, (d) - (f): those for the Ss_0 mode at the beginning part (~1.7 μm-wide IMIMI-W) of the 2nd RT-IMIMI-W with the LSMs, and (g) - (i): those for the Sa_0 at the end part (1.8 μm-wide IMIMI-W) of the 2nd RT-IMIMI-W with the LSMs. Red arrows represent the direction and the strength of the E_z field.

3. Device fabrication

A hybrid structure of the WPMC in Fig. 1 was fabricated by applying the following procedure for easy fabrication. A 25 μm-thick lower clad layer was formed by spin-coating a low-loss UV curable polymer (ZPU-450, supplied by ChemOptics, Inc [31].) with a refractive index of 1.45 at a wavelength of 1.55 μm onto a silicon substrate and then UV curing it. To form the thicker part of the lower Au layer, the corresponding region of the lower clad layer was etched by a depth of 30 nm. Then, a 30 nm-thick Au layer was thermally evaporated and unnecessary regions were removed by a lift-off process. Next, a 20 nm-thick Au layer was again evaporated and patterned by using an Au etchant for the lower 50 nm-thick MIM-W and the lower 20 nm-thick IMIMI-W. To form the 500 nm-thick central insulator layer, another low-loss UV curable polymer resin (ZPU-450-LV500, supplied by ChemOptics, Inc.) with an identical refractive index as the lower clad material was spin-coated and UV-cured. The thickness of the central insulator was measured to be ~500 nm by a surface profiler. Again, a 30 nm-thick Au layer is evaporated and patterned by lift-off process for the upper 50 nm-thick MIM-W. Then, for the 20 nm-thick IMI-W, the upper 20 nm-thick IMIMI-W, and the upper 50 nm-thick MIM-W, a 20 nm-thick Au layer was evaporated. The thicknesses of the Au layers in the IMI-W, the IMIMI-W, and the MIM-W were measured to be ~20 nm, ~20 nm, and ~50 nm, respectively, by an atomic force microscope.

An etching process was carried out for patterning the upper and lower Au layers at a time after the metal layer processes. First, the resin used for the central insulator layer was spin-coated and UV-cured. Then, a 50 nm-thick Cr masking pattern was formed by help of lift-off process. The polymer and Au layers were selectively etched by RIE processes with O_2 and Ar gases up to a depth of ~2.25 μm. After removing the Cr masking pattern with a wet etching process, the selectively etched region was filled by spin-coating and UV-curing a third low-loss UV curable polymer resin (ZPU-450-LV3000, supplied by ChemOptics, Inc.). Then, a 20 nm-thick Cr masking layer was deposited and patterned for LSMs by a lift-off process. Next, the polymer region exposed after the patterning of Cr masking layer was selectively etched by 3.0 μm by using O_2 RIE. After removing the Cr masking layer, a transparent silver ink (TEC-IJ-040, supplied by InkTec Co. Ltd [28].) was spin-coated and thermally sintered. After removing the residue of the silver LSMs, a 25 μm-thick upper clad layer was formed by spin-coating the resin used for the lower clad. The detailed fabrication processes are described in [35].

4. Results and discussions

An IR-Vidicon camera with a 50 × objective lens was used to measure the mode sizes. By using beam-profiling software, the $1/e^2$ horizontal and vertical mode sizes were evaluated by fitting the captured mode images with Gaussian profiles. The mode size for the PMSMF was measured as 10.3 μm × 10.3 μm (horizontal × vertical) at the wavelength of 1.55 μm, as shown in Fig. 5(a). This mode size was used as a reference to calibrate the measured mode sizes. By using the butt-coupling method, the s_0 mode was excited in the 5 μm-wide and 20 nm-thick IMI-W and its mode size was measured to be 10.3 μm × 8.1 μm as shown in Fig. 5(b). The mode size size was squeezed to ~79% (horizontal 100% × vertical 79%) of that in the PMSMF. Then, the s_0 mode was coupled into the Ss_0 mode in the 1.7 μm-wide IMIMI-W via the RT-IMIMI-W as shown in Fig. 5(c). The measured mode size for the Ss_0 mode was 5.1 μm × 3.6 μm, which corresponds to ~22% (horizontal 50% × vertical 44%) of the s_0 mode in the 5 μm-wide IMI-W. At the final stage, the measured mode size of the 1.8 μm-wide and 50 nm-thick MIM-W in the Sa_0MC was 2.9 μm × 2.9 μm as shown in Fig. 5(d). The mode size was squeezed to ~46% (horizontal 57% × vertical 80%) of that of the Ss_0 mode in the 1.7 μm-wide IMIMI-W. Note that the mode size of the Sa_0 mode in the 1.8 μm-wide MIM-W was totally squeezed to ~8% (horizontal 28% × vertical 28%) of that in the PMSMF.

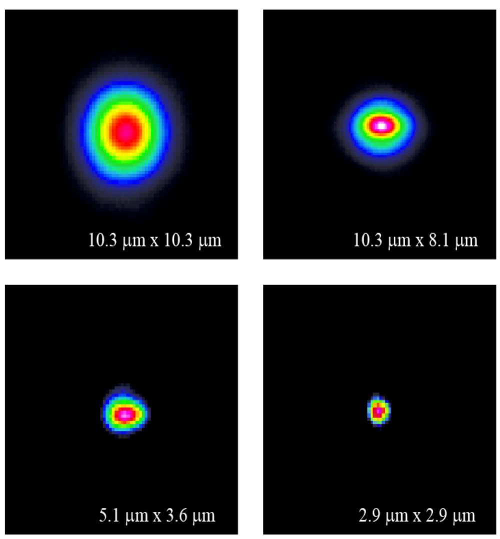

Fig. 5. Optical microscope images of the mode-intensity profiles for the (a) PMSMF, (b) 5 μm-wide IMI-W, (c) 1.7 μm-wide IMIMI-W, and (d) 1.8 μm-wide MIM-W. An IR-Vidicon camera with a 50 × objective lens was used to take the images. The contour colors represent arbitrary values. The horizontal and vertical mode sizes were evaluated by fitting the captured mode images with Gaussian profiles.

It is impossible to take an image of the converted Sa_0 mode with the mode size less than 3.0 μm by using the IR-Vidicon camera because the resolution for the 50 × objective lens is

#169659 - $15.00 USD Received 1 Jun 2012; revised 10 Jul 2012; accepted 24 Jul 2012; published 31 Jul 2012

~3.0 μm. The Sa_0 mode image in Fig. 5(d) is close to the limit of the lens resolution. The simulated mode size in the 1.8 μm-wide MIM-W is 1.1 μm × 0.5 μm as shown in Fig. 3(b), but the measured one is 2.9 μm × 2.9 μm. To confirm the Sa_0 mode in the WPMC, the far-field image of the output mode was simulated and compared with the measured image. Figure 6(a) shows the far-field image calculated by the FDTD simulation with the perfectly matched layers which are absorption boundaries [36]. The spatial resolutions Δx , Δy and Δz are firstly set to 10 nm and the finer meshes are added in the x- and y-directions of the metal regions (e.g., Au strips, LSMs and VSRs), where the resolutions Δx and Δy are 5 nm and 0.5 nm, respectively. The time step Δt is given by $\Delta t = S\,\Delta z\,/c < (1/\sqrt{2})\Delta z\,/c$, and set to 0.02 femtosecond (fs), giving rise to the Courant factor S = 0.6, in order for the FDTD simulation to be stable (not diverge). In the simulation, 4.02×10^{8} nodes are used and the total time simulated is 880 fs. The far-field image shown in Fig. 6(a) is obtained from the output near-field of the Sa_0MC shown in Fig. 6(b), which is used as the input field of the FDTD simulation. Figure 6(c) shows the far-field image measured by the IR-Vidicon camera. The far-field image looks like a diffracted pattern vertically in both the simulation and the measurement. However, this is an indirect proof. To verify the converted Sa_0 mode in the WPMC, a near-field scanning optical microscope (NSOM) is required to take nano-scale mode images because the NSOM provides the sub-wavelength resolution.

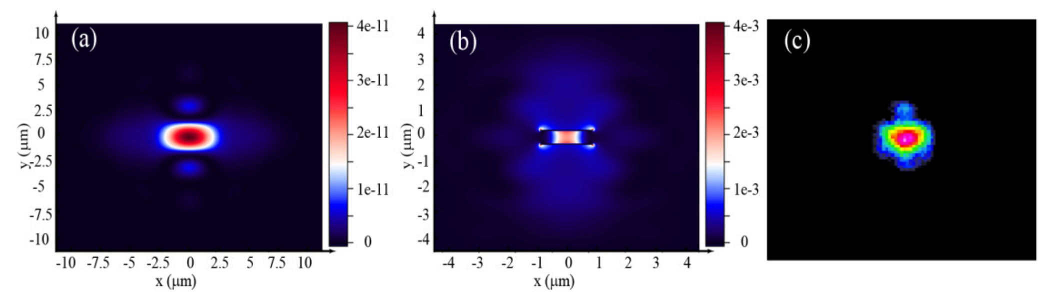

Fig. 6. (a) Far-field image calculated with FDTD, (b) the input near-field image used for the far-field image simulation, and (c) the far-field image measured with the IR-Vidicon camera.

The propagation loss and the coupling loss at each stage was analyzed based on the insertion losses measured at the wavelength of 1.55 μm using a cut-back method. The propagation loss for the 5 μm-wide and 20 nm-thick IMI-W and the coupling loss with the PMSMF were ~5.5 dB/cm and ~0.8 dB/facet, respectively. The loss for the s_0 to Ss_0 mode conversion in the R-PMSC was 1.2 dB in simulation. The propagation losses for the 20 nm-thick and 500 nm-gap IMIMI-W were measured as a function of the width of the Au strips with the range of 2-6 μm. Therefore, the propagation loss for the 1.7 or 1.8 μm-wide and 20 nm-thick IMIMI-W was estimated to be ~50 dB/cm. The loss for the Ss_0 to Sa_0 mode conversion in the Sa_0MC was 5.2 dB in simulation. The propagation loss for the 1.8 μm-wide, 50 nm-thick and 500 nm-gap MIM-W could not be measured because of the limit of the measurement. Therefore, the propagation loss for the MIM-W was simulated and the value is ~0.5 dB/μm. Therefore, the estimated total loss is ~9.5 dB including the conversion loss of ~6.4 dB from the s_0 mode to the Sa_0 mode via the Ss_0 mode and the propagation loss of ~2.3 dB in the WPMC and the coupling loss of ~0.8 dB with the PMSMF. The total loss of the WPMC is not a matter to solve because it is less than ~10 dB. Note that the unit of length of the propagation losses in the IMI-W and the IMIMI-W is cm, but that in the MIM-W is μm.

#169659 - $15.00 USD Received 1 Jun 2012; revised 10 Jul 2012; accepted 24 Jul 2012; published 31 Jul 2012

Table 1. Detailed losses in the WPMC

	5 μm-wide IMI-W	1.7 μm-wide IMIMI-W	1.8 μm-wide MIM-W
propagation loss	5.5 dB/cm[1]	50 dB/cm[2]	0.5 dB/μm[3]
coupling loss[4]	0.8 dB		
conversion loss[5]	1.2 dB		
conversion loss[6]	5.2 dB		

[1]measured value by the cut-back method.
[2]extrapolation from measured values of 2 ~6 μm-wide IMIMI-Ws.
[3]simulated value.
[4]measured coupling loss between PMSMF and 5 μm-wide IMI-W.
[5]simulated conversion loss from the s_0 to Ss_0 mode.
[6]simulated conversion loss from the Ss_0 to Sa_0 mode.

Again, note that the total length of the designed WPMC including the 4 μm-long MIM-W is 53.65 μm. Detailed losses in the WPMC are summarized in Table 1. The proposed WPMC opens a new route for nano-plasmonic integrated circuits with the mode size less than the diffraction limit of light, and furthermore, may be useful for integrating plasmonic, electronic, and conventional photonic devices. This may be applied to overcome the diffraction limit of a light source in nanolithography technology by attaching this module to the exit of the light source.

5. Conclusions

WPMCs are presented at a wavelength of 1.55 μm. The WPMC is composed of the straight IMI-W, the 1st RT-IMIMI-W, the straight IMIMI-W, the 2nd RT-IMIMI-W with the LSMs, and the MIM-W in series. The input mode size of 10.3 μm × 10.3 μm from the PMSMF was squeezed to the measured mode size of ~2.9 μm × 2.9 μm by converting the s_0 mode to the Sa_0 mode via an Ss_0 mode. The measured mode sizes of the s_0, Ss_0, and Sa_0 modes for the 5 μm-wide IMI-W, the 1.7 μm-wide IMIMI-W, and the 1.8 μm-wide MIM-W were 10.3 μm × 8.1 μm, 5.1 μm × 3.6 μm, and 2.9 μm × 2.9 μm, respectively. The mode size of the Sa_0 mode in the 1.8 μm-wide MIM-W was ~8% (horizontal 28% × vertical 28%) of that of the single mode in the PMSMF. The estimated total loss is less than ~10 dB including ~6.4 dB conversion loss from the s_0 mode to the Sa_0 mode via the Ss_0 mode, and ~2.3 dB propagation loss of the WPMC and ~0.8 dB coupling loss with the PMSMF. This WPMC may be useful for bridging micro- to nano-plasmonic integrated circuits.

Acknowledgments

This work was supported by the IT R&D program of the Ministry of Knowledge Economy (MKE), the Korea Evaluation Institute of Industrial Technology (KEIT) (KI001804), and the World Class University (WCU) program through the National Research Foundation of Korea (NRF) funded by the Ministry of Education, Science and Technology (MEST) (R32-2008-000-10204-0).

#169659 - $15.00 USD Received 1 Jun 2012; revised 10 Jul 2012; accepted 24 Jul 2012; published 31 Jul 2012